RSC Sustainability

ROYAL SOCIETY OF CHEMISTRY

PAPER

View Article Online
View Journal | View Issue

Cite this: *RSC Sustainability*, 2026, **4**, 1508

Sustainable approach for the sequestration of lead from water involving the synergistic influence of PET waste and L-cysteine encapsulated in sodium alginate beads

K. Krishna Priyanka,[a] Arunraj Balasubramanian,[b] M. Christina Nilavu,[a] Himanshu Aggarwal *[a] and N. Rajesh *[a]

The toxicity of heavy metals, particularly lead, in water is a significant environmental and health concern. Carbonaceous adsorbent materials derived from waste sources exhibit promising potential for sequestering toxic metals from water. Herein, we developed a sustainable approach using valorised waste polyethene terephthalate (PET) obtained from plastic bottles as a carbonaceous adsorbent material *via* microwave assistance and functionalized it with L-cysteine to incorporate surface functionalities for effective coordination with lead ions. The adsorbent was further encapsulated using a sodium alginate matrix to form a hydrogel, which increased the adsorption capacity and enabled scaling up. Analytical surface characterisations, including FE-SEM, EDS, BET, TGA, XPS, XRF, FT-IR spectroscopy, and PXRD, were performed to study the adsorbent. The maximum adsorption capacity under optimised conditions was found to be 370.84 mg g^{-1}. Kinetic studies revealed that the system follows a pseudo-second-order model, and thermodynamic analysis showed that adsorption is spontaneous and exothermic in nature. The interaction of lead ions with the surface of the adsorbent was further corroborated using molecular dynamics (MD) simulations. The prepared adsorbent was tested in tap water and drinking water, and the adsorbent material exhibited 86.04% and 90.00% removal of lead, respectively. Lead was successfully desorbed using 0.1 M NaOH. In addition to supporting sustainable waste management, this work presents a relatively low-cost, eco-friendly adsorbent system that can serve practical utility in real-world applications for the remediation of lead-contaminated water.

Received 17th January 2026
Accepted 21st January 2026

DOI: 10.1039/d6su00033a

rsc.li/rscsus

Sustainability spotlight

Access to clean water is increasingly challenged by rapid urbanisation and industrialisation. Discharge of effluents that are rich in heavy metal ions without proper treatment can pose serious threats to the environment and health risks to humans and aquatic life, causing neurological disorders, cancers, developmental disorders, and the accumulation of heavy metals in the food chain. Therefore, addressing this pollution is vital to ensure safe, potable water, which is essential for human and aquatic well-being. In this study, we developed a sustainable approach for valorising polyethene terephthalate (PET) from discarded plastic bottles into a functional carbonaceous adsorbent *via* microwave-assisted activation, followed by modification with L-cysteine for lead removal from water. This work fulfils the following Sustainable Development Goals: SDG 6 (clean water) and SDG 12 (responsible consumption).

1 Introduction

Heavy metals are described as elements that are denser than water, with a large atomic radius.[1] Approximately 40% of global fresh waters, lakes and rivers are contaminated with heavy metals.[2] The adverse effects of heavy metals are often pressing due to their persistent half-life, unlike certain organic pollutants, which can degrade over time. These inorganic pollutants are typically challenging to degrade due to their solubility in aqueous media and their ability to form complexes readily with elements such as carbon, nitrogen, and oxygen.[3] They readily bind to biological systems upon consumption and accumulate, posing a significant concern to both human and aquatic life.[4] Lead is the most studied pollutant due to its widespread presence in the environment. The most common sources of lead contamination include mining, industrial effluents (particularly those from lead acid battery manufacturing and pharmaceutical industries), plumbing, agricultural runoff, electroplating, and paint industries. Lead is considered a metabolic poison

[a]*Department of Chemistry, Birla Institute of Technology and Science, Pilani, Hyderabad Campus, Jawahar Nagar, Kapra Mandal, Medchal District, Telangana 500078, India. E-mail: nrajesh@hyderabad.bits-pilani.ac.in; himanshu.aggarwal@hyderabad.bits-pilani.ac.in*

[b]*Maseeh Department of Civil, Architectural and Environmental Engineering, University of Texas, Austin, TX, 78712, USA*

that can cause significant damage to the nervous system, kidneys, liver, and brain and can lead to vertigo, and anaemia. According to the WHO, the permissible limit for lead is 0.05 mg g^{-1}. Over several years, various techniques have been adopted for treating heavy metal ion contamination, including solvent extraction, chemical precipitation, coagulation, membrane filtration, ion exchange resins, and photocatalytic separation.[5] However, these techniques face certain limitations, including higher operation and maintenance costs, energy consumption, lower removal efficiency, selectivity towards one particular ion, and production of harmful secondary waste. Adsorption has emerged as an efficient method for treating wastewater due to its economical and efficient approach to remediation, with very low energy consumption. Several adsorbents have been reported over the years for lead removal, including activated carbon, zeolites, clay, LDHs, MOFs, and agricultural and industrial waste, such as fly ash. Considering the perspective that low-cost carbon-based adsorbents from various sources have been explored, their efficient performance has consistently been recognised owing to their high potential for removing heavy metal ions, making them ideal for scale-up purposes. However, the adsorption capacity of carbon-based adsorbents is often hindered by agglomeration. Encapsulating the adsorbent in sodium alginate can effectively overcome this issue by improving particle dispersion while simultaneously enhancing the overall adsorption efficiency.

Concurrently, a severe environmental problem has been aggravated by the unrelenting expansion of plastic manufacturing and disposal; persistent polymer waste accumulates in landfills and natural systems, posing risks to human health and the environment.[6] Urbanisation, rapid economic development, and increasing population are the primary drivers of plastic waste growth. The specific chemicals used in plastics vary depending on the type of plastic being manufactured or the production process. By converting end-of-life plastics into porous carbons or other advanced materials for environmental applications, one can mitigate the environmental burden of plastics used for value-added purposes. One of the most popular packaging polymers is polyethene terephthalate (PET). One out of every five PET bottles has been identified as non-food grade, but they are widely used due to their excellent physicochemical properties, including electrical and thermal resistance. Its resistance to biodegradation and longevity has led to numerous studies on sustainable methods, including the formulation of value-added reuse techniques. Through chemical activation and regulated carbonisation, PET can be recycled into high-surface-area carbon materials according to recent studies.[7] This offers a promising approach to minimising plastic pollution and creating functional materials for environmental applications.

Combining these two issues presents an appealing solution for a circular economy by converting PET waste into useful carbon adsorbents that are suitable for environmental remediation. In this study, we report a sustainable route that involves the valorisation of PET waste into a porous carbonaceous adsorbent with a high surface area, which is obtained through chemical activation using KOH with microwave assistance.[8] This was further modified by incorporating L-cysteine for improved interaction with the lead. This integrated strategy can effectively tackle two significant environmental challenges, plastic pollution and heavy metal contamination, while aligning with circular economy principles and promoting sustainable water remediation techniques.

2 Materials and methods

2.1 Materials

Lead nitrate (10 099-74-8; extra pure 99%), potassium hydroxide (1310-58-3; extra pure 85%), epichlorohydrin (106-89-8; extra pure 99%), L-cysteine (52-90-4; CHR 99%), and sodium carbonate (497-19-8; anhydrous ACS, 99%) were obtained from SRL (Sisco Research Laboratories, India). Plastic bottles were used as the source of PET. Methanol (HPLC grade) was obtained from Thermo Fisher Scientific India Pvt. Ltd, and nitric acid and hydrochloric acid (extra pure) were obtained from Actylis. Sodium chloride (7647-14-5, extra pure 99%) was obtained from Merck. Potassium dihydrogen phosphate (7778-77-0, extra pure 99%) was obtained from Avra, India. Sodium hydroxide (1310-73-2, extra pure 99%) was obtained from SDFCL (SD Fine Chemicals, India), and Milli-Q water was used throughout the preparation of various solutions. All reagents and chemicals used throughout the study were of analytical grade and were used without further purification.

2.2 Preparation of the adsorbent

PET (Polyethene terephthalate) was obtained from used plastic bottles, which were finely shredded into small pieces and mixed with potassium hydroxide in a 1 : 2 ratio. The mixture was then placed in an alumina crucible, followed by the addition of 1 mL of DI water. The crucible was left in an oven at 80 °C for 6 h. The mixture was cooled and subjected to microwave irradiation (700 watts) for 10 minutes in pulse mode. Then, 50 mg of activated carbon was added to enhance the microwave absorption in the PET. In general, carbon-based materials are utilised in microwave pyrolysis to enhance heat transfer and minimise energy loss due to their high dielectric loss, which hinders the efficient conversion of microwave energy into heat and reduces process efficiency. Activated carbon is not primarily involved in the reaction; instead, it is used to promote rapid and uniform heating of the PET.[9] The obtained black powder was then washed by centrifugation with 0.1 M HCl, followed by DI water until the solution was neutral, and dried in an oven at 80 °C overnight. Oxidation was performed by transferring 1.0 g of the carbon into a round-bottom flask with 50 mL of 5.0 M HNO_3. The mixture was stirred at 80 °C for 4 h, and the carbon was filtered, washed until neutral, and dried overnight at 60 °C. 1.0 g of the oxidised carbon was taken and dispersed in DI water. The pH of the solution was adjusted to 8.0, followed by the addition of 1.0 mL of epichlorohydrin dropwise, and the mixture was allowed to stir at RT for 6 h, which was then filtered. The wet cake was transferred into 50 mL of phosphate buffer solution of pH 7.4, which was prepared by mixing 25 mL of 0.2 M KHP_2O_4, 19.55 mL of 0.2 M NaOH, and 55.5 mL of DI water containing 500 mg of L-cysteine. The mixture was stirred at 40 °C overnight,

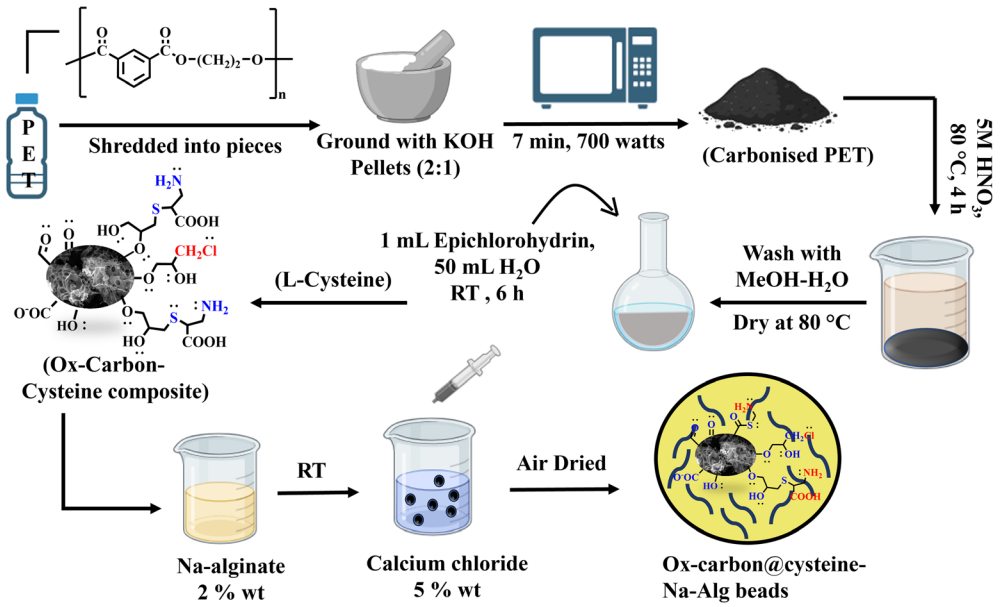

Scheme 1 Preparation of the PET-modified adsorbent material.

after which it was filtered, washed with methanol and DI water, and dried at 60 °C (Scheme 1).

2.2.1 Preparation of sodium alginate beads. Alginate was chosen as the biopolymer matrix due to its biocompatibility; it readily forms stable hydrogel beads under mild aqueous conditions without the need for acids or harsh chemicals. The abundant carboxylate groups enable alginate to actively bind metal ions through various mechanisms, including electrostatic and ion–exchange interactions. Furthermore, alginate beads are stable across a wide pH range and possess sufficient permeability and mechanical integrity, which are often helpful for column adsorption compared to other biopolymers, such as chitosan or cellulose, which usually suffer from pH-dependent solubility or limited metal-binding capacity. A 5% (w/v) alginate solution was prepared by dissolving 1.25 g of sodium alginate in 25 mL of DI water. The mixture was stirred vigorously until homogeneous, followed by the addition of 600 mg of the above-prepared carbon. Stirring was continued at RT for 4 h, after which the solution was dropped into a 10% (w/v) calcium chloride solution to form beads. These beads were cured in a calcium chloride solution for 2 hours to achieve complete crosslinking. Afterwards, the beads were decanted, washed with deionised water, air-dried, and stored in an airtight container for further studies.

2.3 Batch adsorption studies

2.3.1 Preparation of lead solution. A stock solution of lead (1000 mg L^{-1}) was prepared by dissolving 1.6 g of lead nitrate in 1000 mL of Milli-Q water. A calibration curve was obtained (Fig. S1) by preparing a series of concentrations ranging from 2 to 10 mg L^{-1}, which were analysed using atomic absorption spectroscopy (AAS). To perform the batch adsorption experiment, lead solutions were prepared at concentrations ranging from 50 to 500 mg L^{-1} using the stock solution. A 200 mL capacity conical flask containing 0.05 g of the adsorbent and 100 mL volume of the lead solution was used, and the mixture was incubated in an incubator shaker at 230 rpm. The lead concentration before and after adsorption was analysed using AAS; dilution factors were accounted for in all the prepared solutions. The equilibrium adsorption capacity (q_e) of the prepared adsorbents was calculated using the following formula:

$$q_e = \frac{(C_0 - C_e)V}{W}, \quad (1)$$

where C_0 and C_e are the initial and equilibrium concentrations of lead, respectively. V and W represent the volume of the lead solution (L) and the weight of the adsorbent (g), respectively.

2.4 Instrumentation for the analysis of lead and adsorbent characterization

Lead quantification was performed using atomic absorption spectroscopy, AA-7000, Shimadzu, at 283.3 nm. The adsorption process was performed using an incubator shaker (BSI-9) at 230 rpm. An ATR mode Alpha II spectrometer with a DTGS1 detector was used to assess the functional groups of the PET-modified material between 500 and 4000 cm^{-1}; KBr pellets were prepared for the analysis, where KBr was grounded along with the PET-modified material in a ratio of 3 : 1. The morphological and elemental distributions of the prepared material were visualized through SEM-EDS using an FEI Apreo-LoVac scanning electron microscope with Oxford X-Max EDS. The binding energy shift of the elements in the adsorbent was analysed using X-ray photoelectron spectroscopy, which was recorded using a Thermo Scientific K-Alpha (Al-Kα monochromator) XPS instrument. The pH was measured using a Metrohm 867 (Switzerland) module. Thermogravimetric analysis was performed using the Shimadzu DTG-60. The

crystalline/amorphous nature of the PET-modified material was recorded using a Rigaku Ultima-IV X-ray diffractometer with Cu-Kα radiation (1.5405 Å) spread over the 2θ range of 5° to 80°. Surface features were acquired and interpreted through BET analysis using the Microtrac BELSORP Mini II instrument. Contact angle measurements were carried out using the Biolin Scientific-attension theta flex. Stress–strain studies of the prepared alginate beads were carried out using a Universal Testing Machine according to the ASTM D 882 standard, Zwick Roell Z100, with a 5 kN load cell at room temperature.

3 Results and discussions

3.1 Characterisations of the adsorbent

3.1.1 FTIR analysis of the adsorbent. The functional groups and their stretching frequencies of the adsorbent material were analysed using FTIR spectra. The carbon derived from microwave-treated PET (Fig. 1a) exhibits a strong band at around 1590–1600 cm^{-1}, corresponding to the C=C stretching of the carbon domains.[10] A minor band observed between 1200 and 1000 cm^{-1} corresponds to the residual C–O or ester linkages.[11] This may be due to the incomplete PET decomposition. The weak intensities in the O–H and C=O regions indicate that the resulting carbon surface is mainly nonpolar. Upon oxidation with HNO_3 (Fig. 1b), a new pronounced band appeared near 1715 cm^{-1} representing the C=O stretching of carboxylic and carbonyl groups. Peaks between 1220–1050 cm^{-1} were attributed to the C–O stretching of carboxyl functionalities. A broad peak at 3400 cm^{-1} is attributed to O–H stretching,[12] further confirming the incorporation of oxygenated surface groups. After the introduction of epichlorohydrin and grafting with cysteine, visible changes are observed in the IR spectra (Fig. 1c). The epoxide band near 910 cm^{-1} diminishes, indicating ring opening. New peaks arise at approximately 1650 cm^{-1} and 1540 cm^{-1}, corresponding to the amide I (C=O stretching) and amide II (N–H bending) bands, respectively.[13] Owing to the low electronegativity difference between the sulphur and hydrogen, it is often difficult to observe the S–H band in IR. The absorptions between 1250 and 1050 cm^{-1} correspond to C–N and C–O stretching from amino and hydroxyl functionalities.[14] A faint shoulder around 600–700 cm^{-1} arises due to C–S vibrations. After adsorption of lead, there are minor shifts and decreases in the intensity of the 1715 cm^{-1} (carboxyl), 1650 cm^{-1} (amide), and 3400 cm^{-1} (O–H/N–H) peaks, as illustrated in Fig. 1d, suggesting active participation of these groups in metal coordination.

3.1.2 Surface characterisation of the adsorbent. The surface morphology and elemental distributions of the prepared adsorbent were characterised using FESEM and EDS analyses. Before SEM analysis, a thin layer (10 nm) of gold film was uniformly sputter coated over the sample to obtain high-resolution images. Since carbon samples are not conductive, they often lead to charge accumulation and poor resolution images. Scanning electron microscopic characterisation reveals the surface features of the samples in the nanometer range (Fig. 2a–d). The SEM images depict the porous and disordered layered nature of the prepared adsorbent material through microwave carbonisation (Fig. 2a). KOH has a lower lattice energy compared to NaOH; K^+ ions are larger, more mobile, and

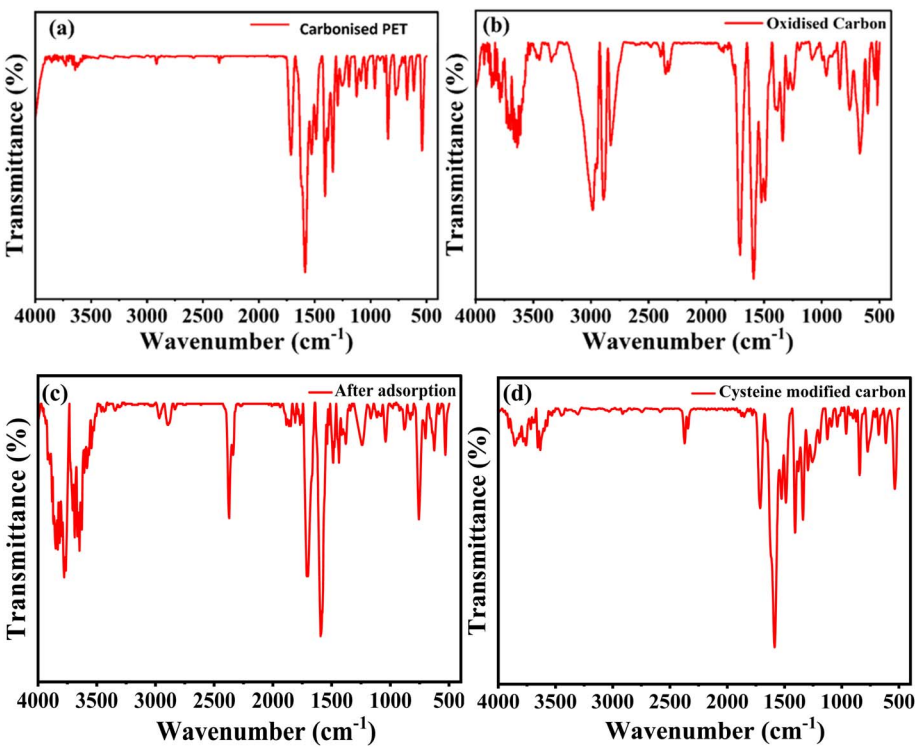

Fig. 1 FTIR spectrum of (a) carbonised PET, (b) oxidised carbon, (c) after adsorption, (d) cysteine-modified carbon.

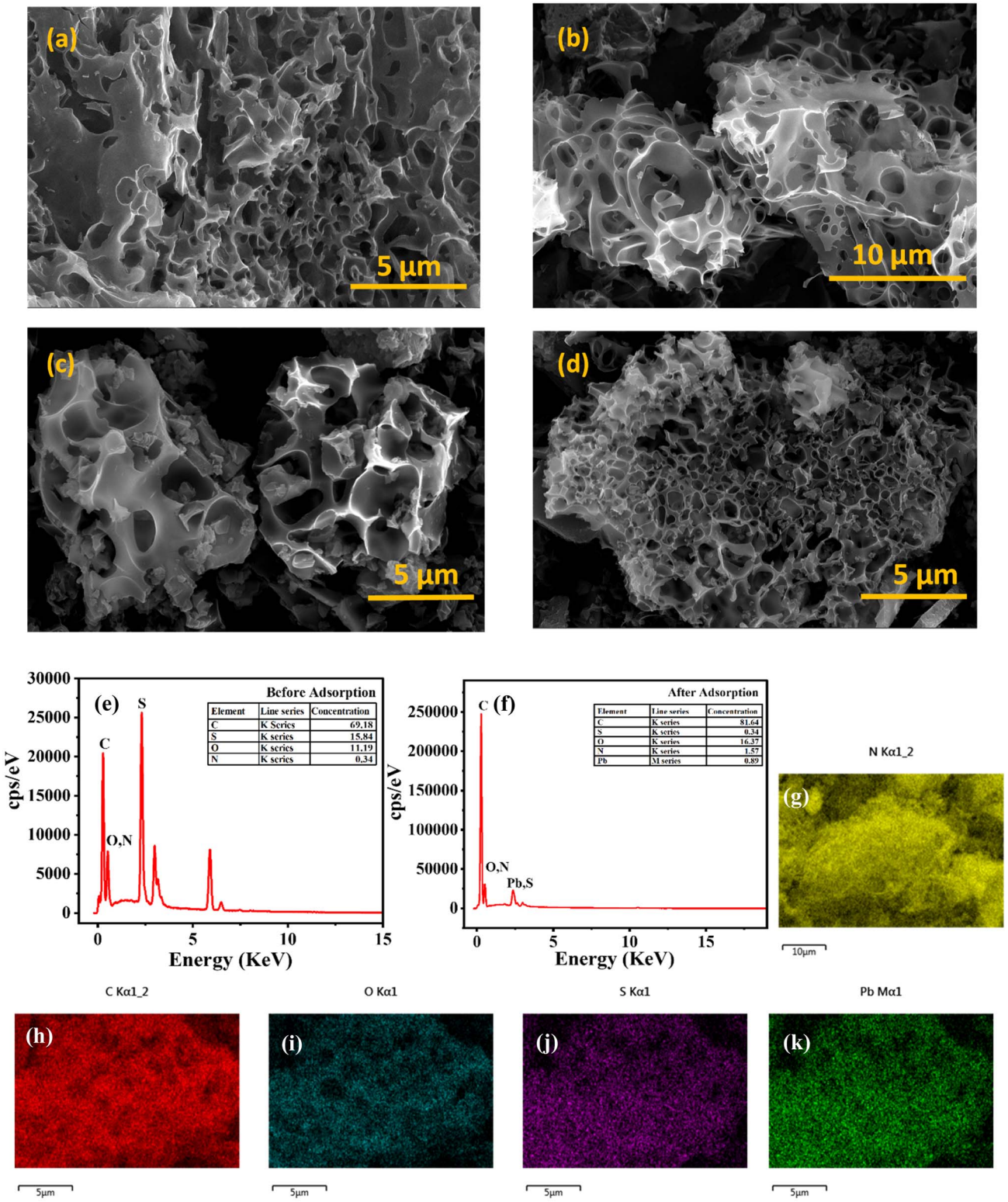

Fig. 2 SEM images of (a) carbonised carbon, (b) oxidised carbon, (c) L-cysteine-modified oxidised carbon, (d) after adsorption, (e) EDS spectra before adsorption (f) EDS spectra after adsorption, (g–k) elemental mapping of C, N, O, S, and Pb after adsorption.

intercalate better into the carbon framework, producing more extensive chemical activation, gas release, and carbon layer expansion. NaOH activation is weaker and tends to leave a denser, less porous material (Fig. S2a–c); hence, KOH was used for activation.[15] There is not much evident change in the surface morphology of the material upon oxidation of the carbonised carbon with nitric acid (Fig. 2b). A certain amount of crystallinity is observed after the introduction of L-cysteine

(Fig. 2c) onto the carbon. EDX spectra and elemental mapping confirm the presence of lead and other elements present on the surface of the adsorbent (Fig. 2e–k).

3.1.3 Thermogravimetric analysis and powder XRD analysis. Thermogravimetric analysis (TGA) is a technique widely employed to study the thermal stability of materials. TGA was performed on the synthesised adsorbent before and after adsorption from RT-800 °C at a rate of 10 °C min^{-1} under a nitrogen atmosphere. It has been observed that the initial mass loss of 6.47% arises due to the residual solvent; the mass loss between 150 °C and 300 °C about 26.9%, is attributed to the decomposition of surface functionalities,[16] such as –COOH, –OH, and –C=O groups, which are introduced during oxidation or modification of the carbon, and due to the decomposition of organic modifiers epichlorohydrin and L-cysteine, a significant mass loss of about 55.2% arises from the oxidation of the carbon matrix. A residual mass of approximately 5–10% observed above 800 °C is due to the formation of a stable inorganic ash and a thermally stable carbonaceous matrix. After the adsorption of lead, the thermal stability of the material increases, as evident from the TGA curve (Fig. 3a), depicting a residual mass of approximately 50% at 800 °C, which is attributed to the formation of thermally stable non-volatile inorganic salts,[17] such as Pb–O or Pb–S. Thus, there is a decrease in the adsorbent's weight loss and an increase in the decomposition temperature, reflecting a strong metal–adsorbent interaction, which confirms successful Pb(II) binding onto the surface.[18] The TGA plot of PET-cyst@Na-alg beads is given in the SI (Fig S5a). The X-ray diffraction pattern of the carbonised carbon (Fig. 3b) exhibited a broad peak around 2θ of 24–26° corresponding to the (002) plane of a poorly disordered graphitic carbon. The absence of sharp peaks indicates the amorphous nature of the carbon.[19,20] Upon modification with L-cysteine (Fig. 3c), the new reflections appear at 2θ = 18.83°, 28.5°, and 34.36°, while the broad (002) peak is reduced. The sharp peaks are attributed to the presence of crystalline sulphur and nitrogen-containing L-cysteine, which increases short-range ordering compared to amorphous carbon. After the adsorption of lead (Fig. 3d), it is observed that the intensity of the peaks in the spectra decreases, which is attributed to the increased absorption of X-rays. It is observed that after adsorption, the *d*-spacing increases from 4.706, 3.12, and 2.6 to 4.718, 3.123, and 2.606, which confirms that some amounts of lead may have intercalated between the adsorbents. However, the peak positions and width remain slightly altered to 2θ = 18.87°, 28.54°, and 34.42°,[21] indicating that the crystallinity of the adsorbent is not significantly altered.

3.1.4 Gas sorption analysis. BET-N_2 isotherm analysis provides information on the surface characteristics of the adsorbent, such as specific surface area, pore diameter, and pore volume, which aids in understanding the mechanism of the adsorption process, specifically the physical adsorption of liquid N_2 (77 K) onto the adsorbent's surface, and provides the basis for analysis. Each of the samples was degassed at 80 °C for

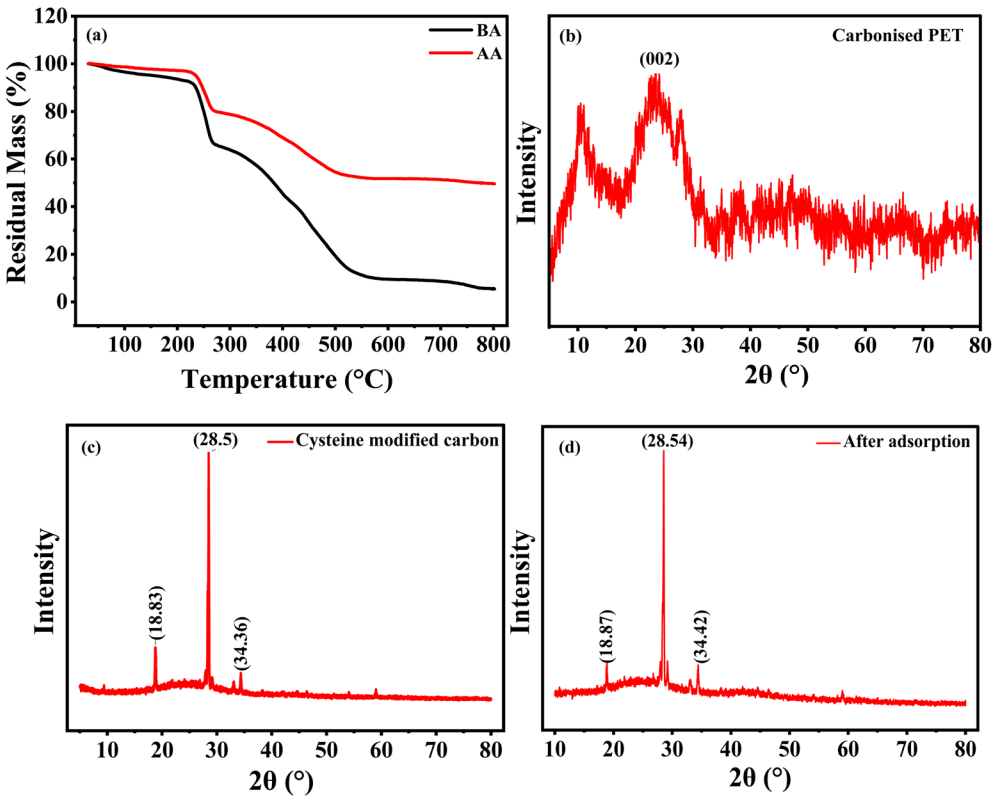

Fig. 3 (a) Thermogravimetric analysis of the adsorbent before adsorption (BA) and after adsorption (AA). PXRD pattern of (b) carbonised carbon, (c) L-cysteine-modified carbon, and (d) adsorbent after lead adsorption.

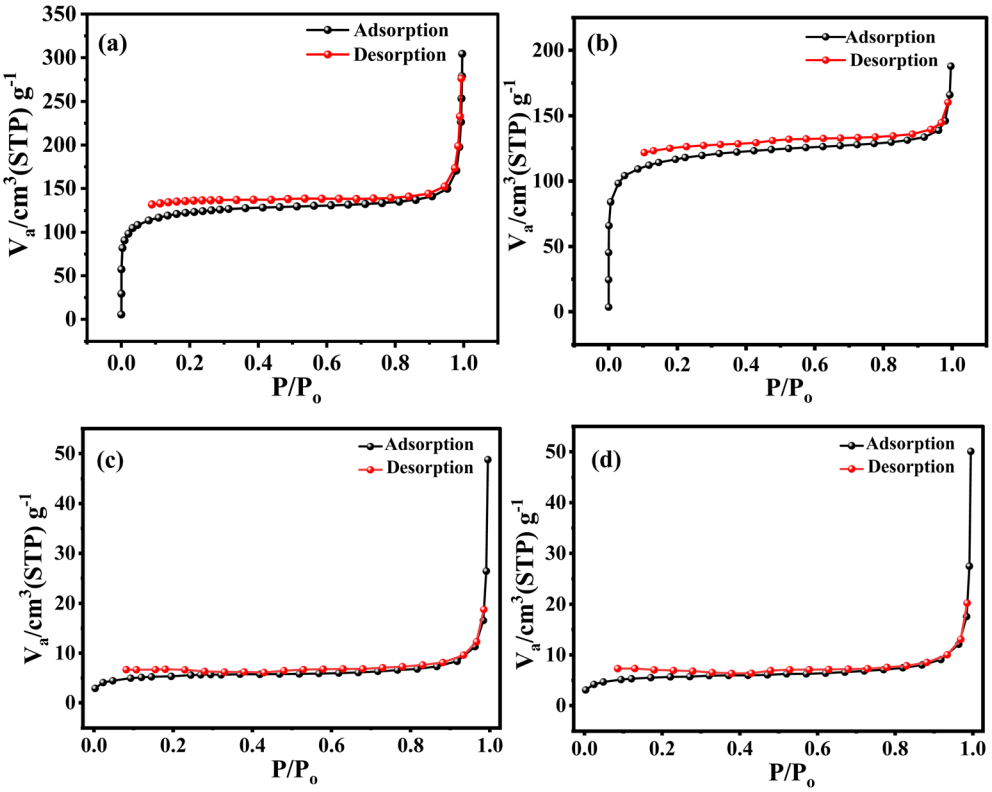

Fig. 4 N_2-adsorption desorption isotherms: (a) carbonised PET, (b) oxidised carbon, (c) L-cysteine-modified carbon, and (d) after the adsorption of lead.

4 h. Fig. 4a shows the N_2 adsorption–desorption isotherm of the PET-derived carbon. It is observed that the material exhibits a Type IV isotherm with capillary condensation at a higher P/P_0; typical of a mesoporous material, the specific surface area was found to be 434.67 m^2 g^{-1}. Upon oxidation with 5.0 M HNO_3, the surface area slightly decreased to 404.85 m^2 g^{-1} (Fig. 4b). The specific surface area of the L-cysteine-modified carbon (Fig. 4c) was found to be 28.2 m^2 g^{-1}. The decrease in surface area is attributed to the usage of epichlorohydrin and L-cysteine for the functionalisation of the carbon. After adsorption (Fig. 4d), it is observed that the surface area decreases further to 14.7 m^2 g,[1] which correlates with the adsorption of lead onto the surface of the adsorbent, leading to a further decrease in the surface area. The pore diameter increased from 12.36 to 20.15 nm, and the pore volume decreased from 0.039 to 0.037 cm^3 g^{-1} owing to the presence of lead after adsorption.

3.1.5 Contact angle and mechanical testing of the adsorbent. To test the hydrophilicity and hydrophobicity of the material, contact angle measurements were performed using an adsorbent material. For simplicity, the beads were converted to thin films during the analysis without altering the ratios. It is observed that the mean contact angle is 59.8° (Fig. S3a), indicating that the material exhibits a hydrophilic nature[22] and is therefore suitable for use in water-based applications. This can be attributed to the presence of polar functional groups, such as –OH, –COOH, –C=O, and –SH, during the oxidation and cysteine modification stages, which increase surface polarity and enhance interactions with water molecules, thereby maintaining the stability of the adsorbent in aqueous media. The mechanical properties of the beads, including tensile stress and Young's modulus, were investigated using a UTM (Universal Testing Machine). For tensile strength,[23] the adsorbent was prepared in the form of a film with a length of 3 cm, and the thickness was found to be 0.16 mm. The analysis was performed using the ASTM D 882 standard. It was observed that the tensile strength of the synthesised adsorbent was found to be 1.41 MPa, and the Young's modulus was calculated to be 63 MPa. From the stress–strain graph (Fig. S3b), it is evident that the breakpoint, *i.e.*, strain at break, was found to be 8.765%. The obtained parameters indicate that the material exhibits a moderately flexible and ductile nature. The low tensile strength is attributed to the porous carbon network with chemical modifications and a crosslinking agent that disrupts the rigidity of the alginate framework at the prepared concentration (5% sodium alginate). However, the strain accommodation is attributed to the carbon material dispersed in the alginate matrix. Overall, the study reveals that the material is a flexible soft polymer composite rather than brittle with a ductile character. These mechanical properties are beneficial for adsorption-based applications because they preserve a large surface area and accessibility of active sites while offering adequate flexibility and structural integrity.

3.1.6 XPS analysis before and after adsorption. X-ray photoelectron spectroscopy is another technique used to

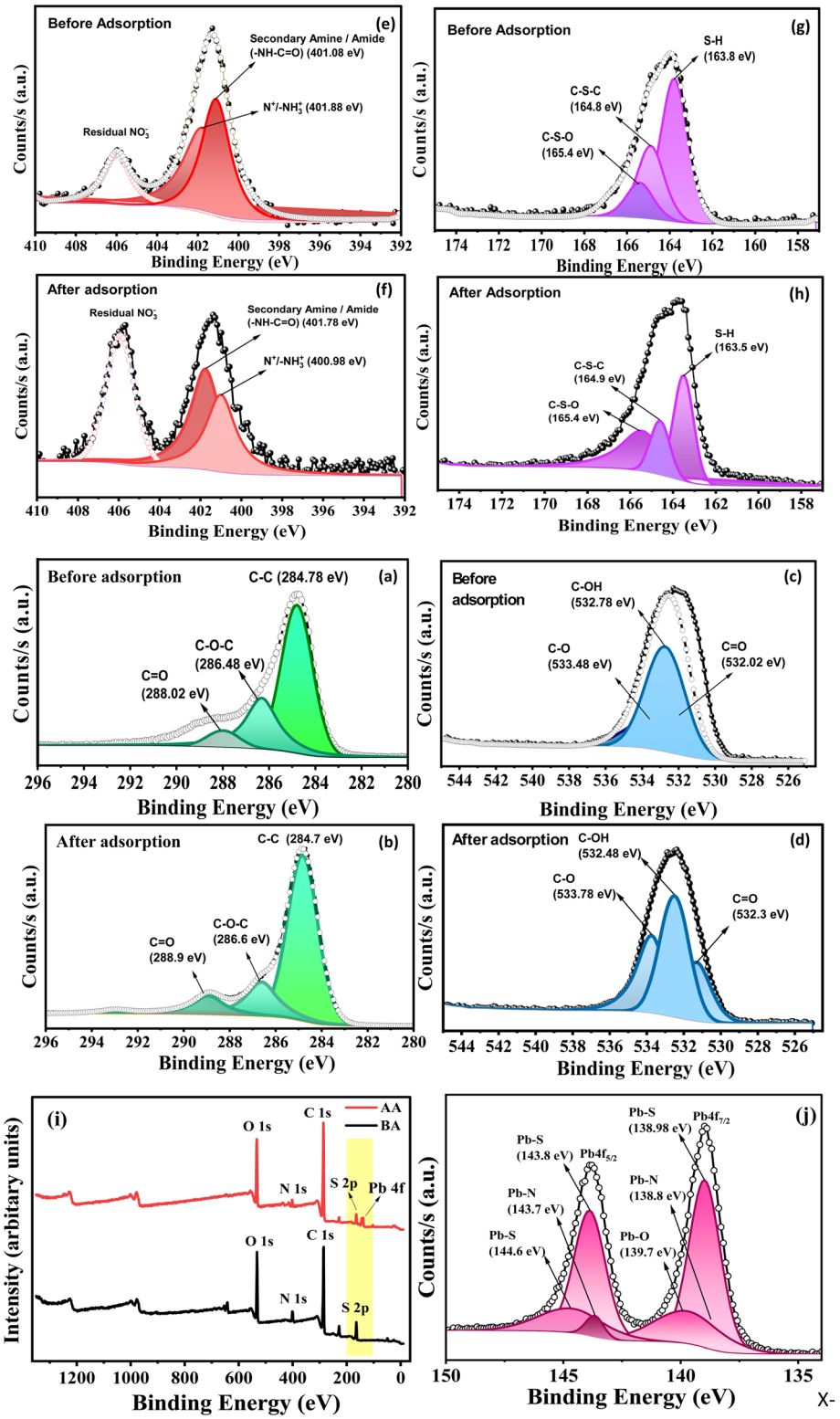

Fig. 5 X-ray photoelectron spectroscopy: (a and b) C 1s before and after adsorption, (c and d) O 1s before and after adsorption, (e and f) N 1s before and after adsorption and (g and h) S 2p before and after adsorption. (i) Survey spectra of the adsorbent and (j) Pb 4f spectrum after adsorption.

study the chemical state of individual elements present on the surface of the adsorbent. In agreement with the EDS spectra, the survey spectrum confirms the presence of C, N, O, and S before and Pb after adsorption (Fig. 5i). The high-resolution C 1s and O 1s spectra (Fig. 5a–d) exhibit binding energy shifts after Pb(II) adsorption, which confirm the chemical interaction between

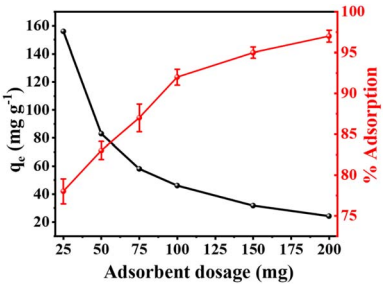

Fig. 6 Adsorbent dosage study; volume: 100 mL and C_0: 75 ppm.

the metal ions and surface functionalities of the adsorbent. It was observed from the C 1s spectrum that the binding energy of C═O increased from 288.02 eV to 288.9 eV, while that of the C–O–C component increased from 286.48 eV to 286.6 eV; no change was observed in C–C. The decrease in binding energy and the increase in binding energy are attributed to the donation of electrons from the carbonyl/carboxyl groups towards the metal centre after Pb(II) adsorption, which increases the binding energy of the carbon.[24] Correspondingly, in the O 1s spectra, the C═O/O–C═O and C–O peaks shifted to higher energies, 532.0 to 532.3 eV and 533.5 to 533.8 eV, respectively, and the binding energy of the C–OH peak decreased from 532.5 to 532.8 eV.[25] These variations arise from the redistribution of electron density upon Pb(II) complexation, confirming that adsorption proceeds predominantly *via* chemisorption through the oxygenated sites on the adsorbent surface. The high-resolution N 1s spectra (Fig. 5e and f) exhibit three components: residual nitrate at 406 eV, a protonated/quaternary N species at 401.0 eV, and an amide/secondary-amine component at 401.8 eV. Upon Pb(II) adsorption, the protonated/quaternary component shifts to a lower binding energy, attributed to the decreased electron density, which is consistent with the electrostatic binding of nitrogen by Pb^{2+}. In contrast, the amide/secondary-amine component shifts slightly to higher BE, which may be due to the electronic reorganisation as a result of the metal adsorption.[26] Due to the large ionic radius of lead, it could possibly interact with the neighbouring functionalities. S 2p spectra (Fig. 5g and h) exhibit shifts of thiol/oxidised-S components, which confirms the interaction of sulphur with the adsorbed lead.[27] The XPS analysis thus illustrates a multidentate adsorption mechanism in which Pb(II) is adsorbed through inner-sphere coordination to oxygen and nitrogen donors, along with electrostatic interactions, and the sulphur groups enhance the binding specificity and stability of the adsorbent.

3.2 Experimental variables

3.2.1 Effect of adsorbent dosage. The effect of adsorbent dosage on lead removal was optimised by performing batch adsorption with varying amounts of the adsorbent, ranging from 50 to 200 mg, in 100 mL of a 75 mg g^{-1} lead solution. It is observed that as the dosage increased from 50 to 200 mg, the adsorption percentage increased (Fig. 6), which can be attributed to the increase in the number of available sites; however, the adsorption capacity decreased due to the saturation of the adsorption sites and the possible agglomeration of the adsorbent particles at a higher dosage.[28] Therefore, 50 mg of the adsorbent was chosen as the optimal dosage, as it provides a good balance between adsorption percentage and efficiency while maintaining the material economy. It was observed that there was only a marginal increase in the adsorption percentage above this dosage, which could not justify the substantial increase in material usage corresponding to the decreasing efficiency.

3.2.2 Effect of pH on the adsorption of lead and the ZPC study of the adsorbent. The pH plays a crucial role in determining the speciation of metal ions in water, thereby influencing their adsorption. To determine the pH at which the maximum adsorption capacity of the synthesised adsorbent is obtained, adsorption studies were performed by adjusting the pH of the lead solutions at a fixed concentration, dosage, volume (50 mg g^{-1}, 50 mg, 100 mL), from 2 to 7 using 0.1 M HCl and 0.1 M NaOH for 6 h in an incubator shaker at 230 rpm. It is observed that maximum adsorption occurs at a pH of 7 (Fig. 7a). At lower pH levels, the surface of the adsorbent is protonated due to the increased H^+ ion concentration, which competes with the metal cation and reduces the adsorption of lead.[29] Electrostatic repulsions also further lower the uptake of Pb^{2+}. As the pH increases, the surface carboxyl (–COOH), hydroxyl (–OH), and thiol (–SH) groups of the cysteine-modified carbon are

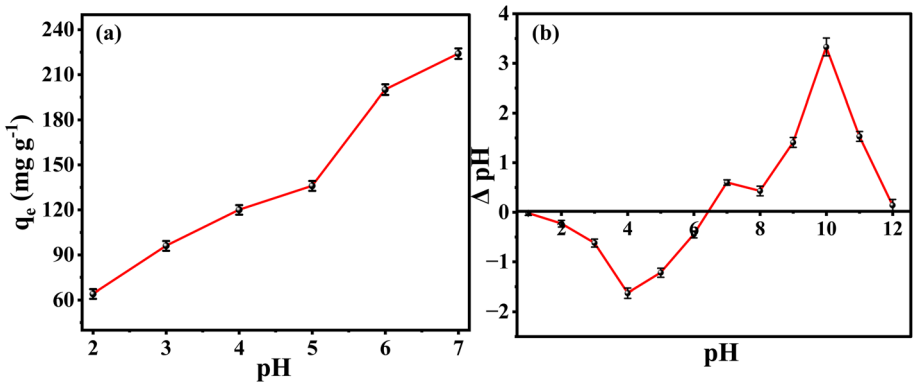

Fig. 7 (a) pH study of the adsorbent (volume: 100 mL, C_0: 50 ppm). (b) Zero point charge of the adsorbent.

effectively deprotonated, which increases electrostatic attraction with Pb^{2+} ions. Above pH 5, the adsorption of lead increases due to the complexation of lead through the deprotonated surface functional groups of the adsorbent (Pb–O and Pb–S interactions). The zero-point charge (ZPC) study was performed using the pH drift method. A stock solution of 0.1 M sodium chloride was prepared, and 25 mL of this solution was transferred into 12 different vials. The pH of each vial was adjusted using 0.1 M HCl and 0.1 M NaOH, ranging from 1 to 12. An equal amount of the adsorbent was added to all the vials and equilibrated for 24 h. The pH of the solution was tested after equilibration and plotted against the initial pH to obtain the ZPC of the adsorbent (Fig. 7b). The isoelectric point was observed to be 6.42. Thus, at a pH below 6.42, the surface of the adsorbent is positively charged, causing electrostatic repulsion of the cation, and at a pH above 6.42, the surface of the adsorbent is negatively charged, increasing the interaction of the cation with the adsorbent, which can be well correlated with the increase in adsorption percentage at pH 7; cysteine exists in a zwitterionic form at this pH, where the carboxyl groups are deprotonated, the amine groups are weakly protonated, and the thiol remains neutral. As cysteine is predominantly grafted through its carboxylate groups, the rest of the amine and thiol groups are exposed on the surface of the adsorbent. Although the grafted cysteine is overall neutral to weakly positively charged at pH 7, the overall surface still retains a negative charge due to the other oxygen-containing functional groups on the carbon and the carboxylate-rich alginate hydrophilic framework, which facilitates the transport and immobilisation of lead through coordination with thiol and weak auxiliary interaction with the amine groups, resulting in synergistic adsorption. Alginate is composed of mannuronic and guluronic acid units with carboxylate groups that have pK_a values in the range of 3.4–3.7. Below this pH, the carboxylate groups are predominantly protonated due to the increased H^+ concentration, which weakens the network and reduces the accessibility of active binding sites, thereby reducing Pb^{2+} uptake. As the pH rises above the pK_a, carboxylate groups deprotonate, which increases the negative charge and enhances electrostatic and ion–exchange interactions, thereby enabling metal ion adsorption.

The adsorption studies were restricted to pH $\leq$ 7 as Pb^{2+} ions tend to hydrolyse and precipitate as $Pb(OH)_2$ or $Pb(OH)_3^-$ species at higher pH, which could cause an error during the estimation of the adsorption percentage. Thus, a pH of 7 is required to maintain lead in a soluble form.[30]

3.3 Adsorption isotherm

The adsorption capacity of the adsorbent was determined through adsorption isotherm studies. Adsorption was carried out by taking 50 mg of the adsorbent in 100 mL of a lead solution of varying concentrations and equilibrating for 6 h at RT. The obtained data were fitted into different linear Isotherm models (Fig. 8a–d), namely Langmuir, Freundlich, Temkin and SIPS isotherms, to interpret the mechanistic view and interactions of the adsorbate with the adsorbent. The Langmuir model assumes monolayer adsorption, while the Freundlich model assumes multilayer adsorption on a heterogeneous surface. The linear equation for the Langmuir isotherm model is[31]

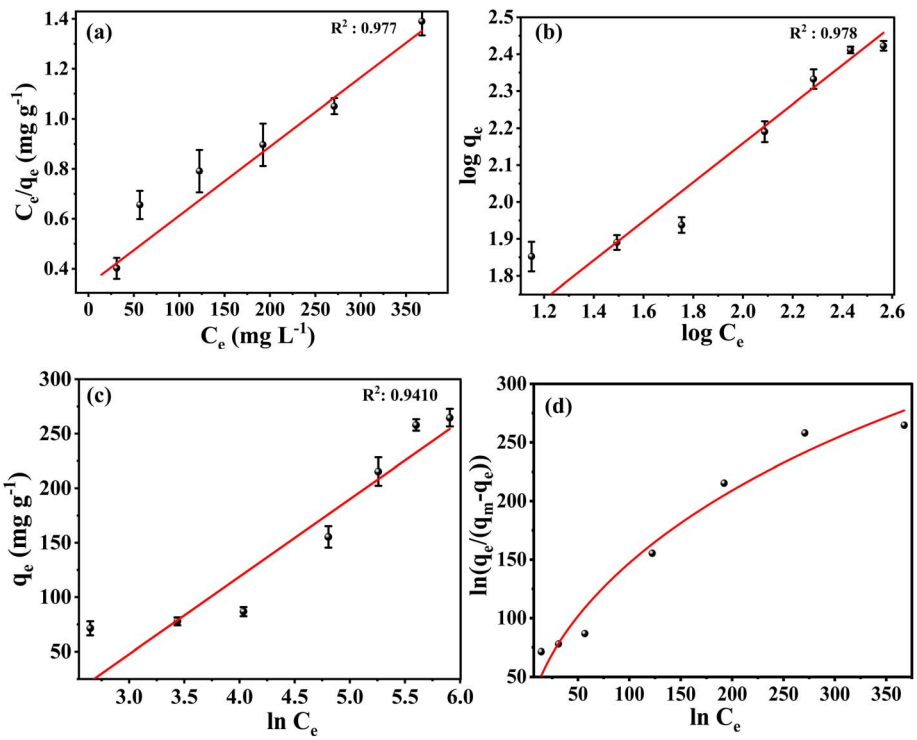

Fig. 8 Adsorption isotherms: (a) Langmuir, (b) Freundlich, (c) Temkin, and (d) non-linear SIPS (weight: 50 mg, volume: 100 mL).

$$\frac{C_e}{q_e} = \frac{1}{q_{max}} C_e + \frac{1}{K_L\, q_{max}} \quad (2)$$

where C_e represents the equilibrium concentration (mg L^{-1}), q_e represents the equilibrium adsorption capacity (mg g^{-1}), q_{max} is the maximum adsorption capacity (mg g^{-1}), and K_L is the Langmuir constant (L mg^{-1}). The Langmuir plot is obtained by plotting $\frac{C_e}{q_e}$ *vs* C_e, where the slope is $\frac{1}{q_{max}}$. The maximum adsorption capacity of the adsorbent, obtained from the linear plot, is 370.84 mg g^{-1}. The linear equation for the Freundlich isotherm model is[32]

$$\log\ \ q_e = \log\ K_F + \frac{1}{n} \log\ C_e \quad (3)$$

where K_F is the adsorption capacity ($mg^{1-1/n}\ g^{-1}\ L^{1/n}$) and n is the constant obtained by plotting the experimental data in the linear Freundlich plot, $\log q_e$ *vs.*$\log C_e$. Here, K_F is the intercept, and $1/n$ represents the slope; n represents the adsorption intensity that should lie between 1 and 10.[33] The calculated n value, as shown in Table S1, indicates favourable adsorption. Dimensionless constant R_L represents the nature of the adsorption, as illustrated in eqn (4). $R_L = 1$ it is considered as linear $R_L = 0$; irreversible adsorption, $R_L > 1$ unfavourable, and when $0 < R_L < 1$ it is considered a favourable process. The calculated R_L value was found to be 0.7, confirming favourable adsorption.

$$R_L = \frac{1}{1 + C_0 K_L} \quad (4)$$

The Temkin isotherm excludes higher and lower concentrations; it considers that the heat of adsorption of the adsorbate molecules on the surface reduces as they are adsorbed onto the surface of the adsorbent. Its linear equation is[34]

$$q_e\ = \frac{RT}{b_{Te}} \ln\ K_T + \frac{RT}{b_{Te}} \ln\ C_e \quad (5)$$

where b_{Te} is the Temkin constant, which explains the heat of adsorption in J mol^{-1}; K_T is the Temkin isotherm constant in L g^{-1}; R is the gas constant at 8.314 J mol^{-1} K^{-1}; and T is the temperature in K.A plot of q_e *vs.* $\ln C_e$ gives us the Temkin plot from which the slope RT/b_{Te} and the intercept $RT/b_{Te} \ln K_T$ are obtained. The Sips isotherm combines the Langmuir and Freundlich isotherms. This three-parameter model follows the Langmuir isotherm at higher concentrations and the Freundlich isotherm at lower concentrations of the adsorbate. Its nonlinear equation is

$$q_e = \frac{q_m (K_S C_e)^{\frac{1}{n_S}}}{1 + (K_S\ C_e\ )^{\frac{1}{n_S}}}, \quad (6)$$

where q_e is the amount of adsorbate adsorbed per unit of the adsorbent at equilibrium, C_e is the equilibrium concentration of the adsorbate, q_m is the maximum adsorption capacity, K_S is the Sips isotherm constant, and n_S is the Sips exponent, a constant that indicates the heterogeneity of the system. A plot of q_e *vs.* C_e gives us the K_S and n_S values, where K_S represents the affinity of the adsorbent to the surface of the adsorbate. When $n_S = 1$, the model simplifies the Langmuir model. A value of $n_S < 1$ indicates that the surface is heterogeneous, while $n_S > 1$ suggests that the adsorption is cooperative. Regression coeffecients of Langmuir, Freundlich, and Temkin models were close, 0.9778 and 0.977, respectively, and that of the nonlinear Sips isotherm was found to be 0.966 (Table S1), indicating that monolayer adsorption, along with some multilayer adsorption, predominates. A certain amount of heterogeneity is observed due to the different functional groups present on the surface of the adsorbent. As observed from the SIPS isotherm, the SIPS isotherm constant (n) obtained was 0.56. The value of n from the Freundlich isotherm reflects variations in the adsorption energy across different adsorption sites. Furthermore, this suggests that lead uptake occurs through various types of interactions. The b_T value of 40 KJ mol^{-1} obtained from the Temkin isotherm reveals that the adsorption process is physico-chemical in nature, which involves strong physisorption, like electrostatic attraction and a moderate to strong chemisorption involving ion exchange and complexation.

3.4 Adsorption kinetics

The adsorption capacity at various time intervals was monitored to gain an understanding of the reaction rate and the interaction of lead with the adsorbent. The adsorption kinetics were performed at a constant temperature with a dosage of 50 mg, a concentration of 50 ppm and a volume of 100 mL. The concentration of lead was measured at regular intervals, and the experiment was conducted until saturation. It was observed that the equilibration attained saturation after 9 h. The obtained data were fitted into pseudo-first-order and pseudo-second-order models. The linear equations for these models are given below.[35]

$$\log(q_e - q_t) = \log\ q_e - \left(\frac{k_1}{2.303}\right) t \quad (7)$$

$$\frac{t}{q_t} = \frac{t}{q_e} + \frac{1}{k_2 {q_e}^2} \quad (8)$$

where q_e (mg g^{-1}) and q_t (mg g^{-1}) represent the equilibrium adsorption and adsorption capacity at time t (min), respectively. k_1 and k_2 are the equilibrium constants for the pseudo-first-order and second-order models, respectively. The pseudo-first-order model is a plot of t *vs.*$\log(q_e - q_t)$, and the pseudo-second-order model is a plot of t *vs* $\frac{t}{q_t}$. By comparing the R^2 values (Table S2), it was observed that the best fit was obtained for the pseudo-second-order model (Fig. 9a and b), correlating with the gradual saturation of the adsorption over time. Here, the adsorption rate is proportional to the square of the unoccupied sites on the adsorbent's surface, a characteristic of chemisorption due to the presence of various functional groups on the adsorbent, which involves ion exchange, chemical coordination, or complexation with the adsorbate molecule. Adsorption enthalpy values below −20 kJ mol^{-1} are attributed to weak physical interactions, while values exceeding −60 kJ mol^{-1} are often associated with chemisorption. The enthalpy change obtained in this study falls within the

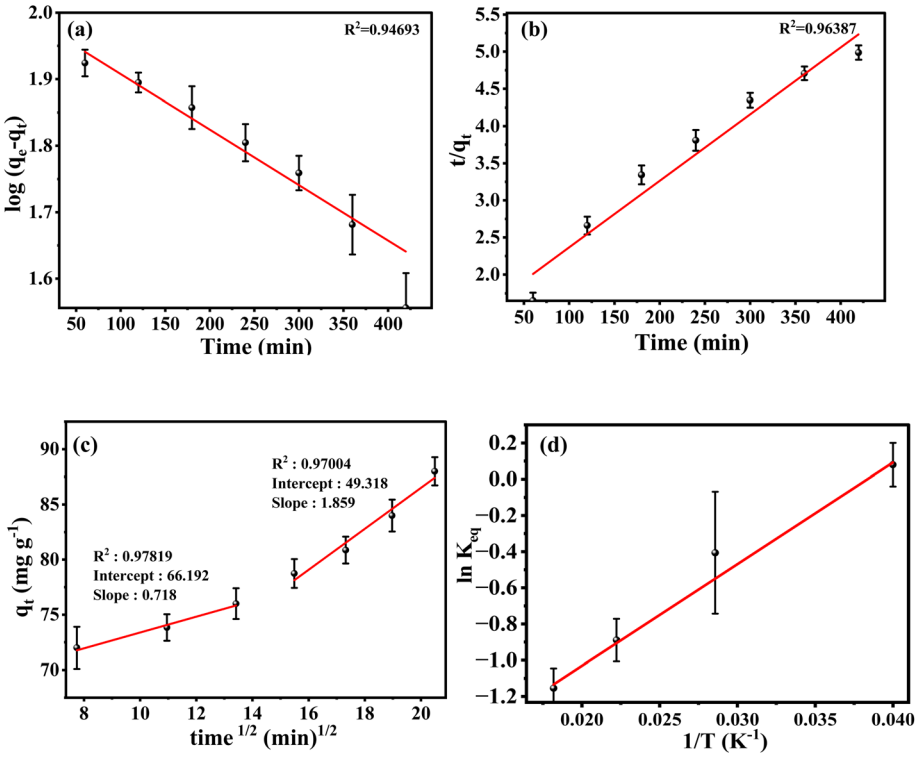

Fig. 9 Adsorption kinetics: (a) pseudo-first-order, (b) pseudo-second-order, and (c) intraparticle diffusion model. (d) Variation in ln K_{eq} against the reciprocal of temperature (Kelvin).

intermediate range, indicating a physicochemical adsorption process that involves both strong physisorption and chemical interactions. Given the heterogeneous nature of the adsorbent, Pb^{2+} uptake is governed by multiple interactions, including surface complexation, ion exchange, electrostatic interactions, chelation, and pore diffusion. Consequently, the measured enthalpy represents a combined thermodynamic effect arising from both physical and chemical interactions.

The intraparticle diffusion model determines the uptake of lead ions (Webber–Morris plot), where it is evident from the graph that adsorption occurs through multiple steps: initial rapid external surface adsorption, diffusion through the boundary layer and film diffusion, where the lead ions are transferred to the adsorbent surface from the bulk, followed by the slower step of the pore diffusion and interaction of the lead ions with the surface functional groups of the adsorbent. It is evident from the slope of the two stages that both mass transfer and intraparticle diffusion are effective during the adsorption process.[36] The linear equation is[37]

$$q_t = t^{0.5}\, k_i + C \tag{9}$$

where k_i denotes the intra-particle diffusion rate constant (mg g^{-1} $min^{-1/2}$) and C represents the thickness of the boundary layer obtained from the intercept of the plot.

3.5 Adsorption thermodynamics

The effect of temperature on the adsorption and its spontaneity is obtained. The study was performed by adding 50 mg of adsorbent to a 100 mL lead solution of fixed concentration and equilibrating it for 6 h at different temperatures: 298.15 K, 308.15 K, 318.15 K, and 328.15 K (Fig. 9d). After this, the concentration was analysed using AAS. The obtained data were fitted into a van't Hoff plot, which quantified how the equilibrium of the adsorption process changed with respect to temperature, thereby determining its feasibility by measuring $\Delta G°$ (kJ mol^{-1}), $\Delta H°$ (kJ mol^{-1}), and $\Delta S°$ (kJ mol^{-1} K^{-1}). The $\Delta H°$ (kJ mol^{-1}) and $\Delta S°$ (kJ mol^{-1} K^{-1}) are obtained from the slope and intercept of the plot ln K_{eq} *vs* $\frac{1}{T}$. The linear equation is

$$\ln K_{eq} = \frac{-\Delta H^\circ}{R}\left(\frac{1}{T}\right) + \frac{-\Delta S^\circ}{R} \tag{10}$$

$$\Delta G^\circ = -RT \ln K_{eq}, \tag{11}$$

where K_{eq} is the equilibrium constant, which provides the ratio of lead ions on the surface of the adsorbent to those in the solution phase. The $\Delta H°$ (kJ mol^{-1}) and $\Delta S°$ (kJ mol^{-1} K^{-1}) are calculated from the slope and intercept of the plot ln K_{eq} *vs* $\frac{1}{T}$. The thermodynamic parameters obtained (Table S3) indicate that the process is spontaneous with a negative $\Delta G°$, indicating favourable adsorption. The negative $\Delta H°$ (kJ mol^{-1}) suggests that the process is exothermic in nature and is accompanied by a decrease in entropy, which can be attributed to the strong interactions of lead with the functional groups of the adsorbent and alginate-bound Ca^{2+}, causing an ordered surface configuration, consistent with the negative $\Delta S°$. The magnitude of $\Delta H°$

was found to be −34.11 kJ mol^{-1}, indicating that the process supports physicochemical adsorption.

3.6 Adsorbent regeneration

Regeneration is a critical aspect of adsorption, which enables us to determine the practical applicability of the synthesised adsorbent material. Materials with higher recyclable potential are always aimed for. To evaluate the reusability of the prepared adsorbent, desorption analysis was performed using 0.05 M and 0.1 M NaOH solutions. It was observed that an efficient result was obtained with 0.1 M NaOH, attributed to the increase in the hydroxide ion concentration disturbing the interaction of lead with the functional groups on the surface of the adsorbent, thereby demonstrating the desorption of lead at a lower concentration. The amount of hydroxide ions released was not sufficient to compete with the lead ions bound to the adsorbent. Hence, 0.1 M NaOH was used as the desorbing agent. Desorption was performed by transferring the adsorbent (50 mg) from the adsorption vessel into a 100 mL conical flask, followed by the addition of 100 mL of 0.1 M NaOH. Desorption equilibrium was attained within 3 hours. 87.6% desorption was observed over the first cycle. The concentration of lead was measured using AAS, with 0.1 M NaOH used as the blank. The material exhibited good stability for up to 5 cycles (Fig. 10). The concentration of adsorbed and desorbed lead decreased slightly over the cycles, which can be attributed to the saturation of the adsorbent's sites. During the desorption of lead using 0.1 M NaOH, Pb^{2+} ions are released from the adsorbent into the basic solution as soluble hydroxy complexes. From a sustainability perspective, the desorbed lead can be conventionally recovered by adjusting the pH to precipitate it as hydroxide or carbonate, followed by filtration, and the solution can be further diluted to well below the permissible limit (sub-ppb levels) and preserved prior to safe subsequent disposal. In this way, higher concentrations of lead would not be released into the environment, aligning with a sustainable approach. Indeed, in a few of our experimental optimisation variables, we also reused the desorbed lead solution for further adsorption studies, aligning with the circular economy as well.

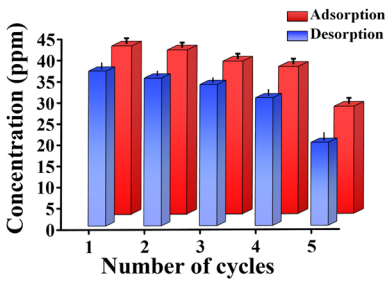

Fig. 10 Adsorption–desorption cycles of the adsorbent (C_0: 50 ppm; vol: 100 mL).

3.7 Fixed-bed column study for lead adsorption

To assess the efficiency of the synthesised beads in treating a higher volume of lead solutions, a fixed-bed adsorption column study was conducted. The prepared beads were packed in a column, 30 cm in height and 2.0 cm in internal diameter, which was filled with 2.0 g of the adsorbent. The beads were filled to a height of up to 3.0 cm, and 200 ppm of lead solution was allowed to pass through the column until it reached saturation. The flow rate was maintained at 2 mL min^{-1}. The experimental data obtained were fitted into two models, the Thomas model and the Yoon–Nelson column model, whose linear equations are as follows:

$$\ln\left(\frac{C_0}{C_t}-1\right)=\frac{K_{\mathrm{Th}}q_0x}{Q}-K_{\mathrm{Th}}C_0t, \tag{12}$$

$$\ln\frac{C_t}{C_0-C_t}=K_{\mathrm{yn}}t-\tau K_{\mathrm{yn}}, \tag{13}$$

where C_t is the concentration of lead at time t, C_0 is the initial concentration of lead, K_{Th} is the Thomas rate constant, the flow rate is represented by Q, and x is the weight of the adsorbent. τ is the time at which 50% of the lead is adsorbed. Column parameters obtained from the experiment are illustrated in Table S5. These are mathematical two-parameter models that are used to understand the kinetics of column adsorption. The breakthrough point from the breakthrough curve was observed to be 240 min, and it attains saturation at 530 min. The maximum adsorption capacity obtained from the fixed-bed

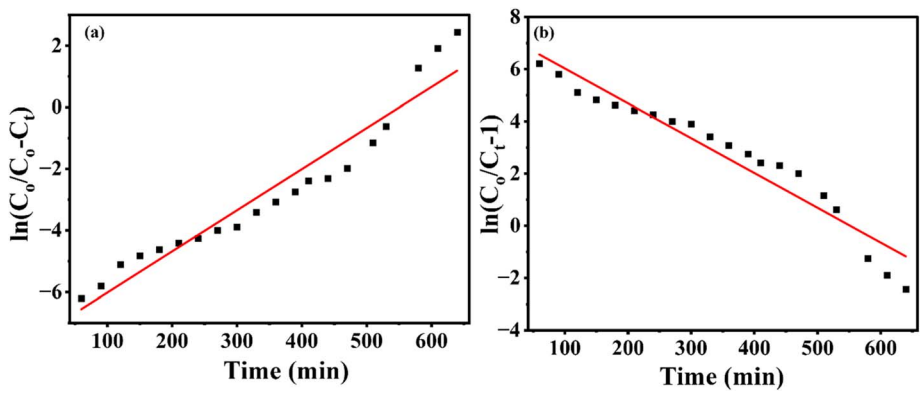

Fig. 11 Linear plot of (a) Thomas model and (b) Yoon–Nelson model.

column was found to be 245.33 mg g^{-1}. τ was found to be 254.55 min (Fig. 11). Adsorption occurs through diffusion, followed by mass transfer. After the adsorbent attains saturation, the column was washed with 0.1 M NaOH to confirm the desorption of lead. Each fraction of lead was analysed using AAS during the column study and after desorption. Since the synthesised adsorbent material was converted into bead form, column packing and regeneration were straightforward, making the process highly suitable for large-scale or industrial applications.[38]

3.8 Mechanistic view of adsorption

During the microwave carbonisation of PET, KOH is used as both an activating agent and an initiator for the decomposition of the polymeric matrix when exposed to microwave irradiation. This process degrades the ester bonds to form terephthalate, which, at higher temperatures, condenses to form disordered carbon residues. The formation of K_2CO_3 and metallic K occurs through the reductive decomposition of KOH, which etches the carbon framework to generate mesopores or micropores.[39]

$$6\ KOH + 2C \rightarrow 2K + 3H_2 + 2\ K_2CO_3 \quad (14)$$

Oxidation with 5.0 M HNO_3 introduces various functional groups onto the surface, including (–COOH, –OH, and –C=O) through oxidative cleavage of the disordered carbon matrix. The higher the concentration of the nitric acid used and the longer the exposure duration, the higher the density of acidic functionalities introduced onto the carbon surface.[40] As a result, the carbon becomes increasingly hydrophilic. This process removes any remaining potassium left behind during the activation process, which could potentially block pores. Epichlorohydrin consists of an epoxide ring and a chlorine group under basic conditions (pH 8). Surface –OH groups are deprotonated, which likely causes them to attack the less hindered side of the carbon, thereby opening the ring. As a result, a glycidyl ether linkage is formed between epichlorohydrin and the surface of the carbon.[41] During the coupling of L-cysteine in phosphate buffer at pH 7.4, the thiol groups of cysteine act as nucleophiles, substituting for the Cl^- groups through the SN_2 mechanism and leading to covalent grafting of L-cysteine (Fig. 12). As a result, the surface now consists of exposed amino and carboxyl groups from cysteine, creating a multifunctional surface that enables electrostatic and ion exchange interactions,[42] along with a chelating interface. Incorporation of the material into an alginate matrix, which is a polyanionic polymer, is a promising approach in view of the rich presence of oxygen functionality. Hence, it has a favourable interaction with Pb^{2+}, and it also enhances stability and facilitates electrostatic and ion exchange interactions. Lead can undergo electrostatic attraction with the deprotonated $–COO^-$ sites on the alginate and cysteine residues, as well as ion exchange with the Ca^{2+} matrix (Fig. 13). To verify the ion exchange mechanism, the released Ca^{2+} was measured using AAS during the adsorption of Pb^{2+}. A calcium chloride stock was prepared by dissolving 0.25 g of calcium chloride in 100 mL of water, and 2 mL of conc. HCl was added to increase the solubility of the salt. Calibration was performed for concentrations ranging from 0.2 ppm to 1 ppm, and a linear calibration plot was obtained. After the adsorption of Pb^{2+} was carried out using 10 ppm of Pb^{2+} solution, the amount of calcium released was measured using AAS. The results obtained are presented in Table 1. The obtained results indicate a net release of 0.083 ppm of Ca^{2+}. This increase in calcium concentration directly provides experimental evidence for the Ca^{2+}-Pb^{2+} ion exchange that occurred during adsorption. It can be observed that there was no stoichiometric Ca^{2+}-Pb^{2+} exchange, as this mechanism is one of the contributing factors for the adsorption of Pb^{2+}, along with the other possible interactions. During chelation and surface complexation, Pb^{2+} coordinates with the lone pairs of –SH and $–NH_2$, forming Pb–S and Pb–N bonds. Ion exchange involves the exchange of lead with H^+/Na^+ ions at carboxylate sites. Pore diffusion can also occur, as is evident from the multistep adsorption behaviour described by the intraparticle diffusion model. Therefore, adsorption is driven by favourable coordination between lead and the surface functional groups, apart from physisorption, as evident from the thermodynamic parameters.

Table 1 Calcium release before and after the adsorption of lead

Sl. no		Concentration of Ca^{2+} (ppm)
1	Before adsorption	0.09
2	After adsorption	0.182

3.9 Application of real water samples and selectivity studies

To test the efficiency of the synthesised L-cysteine-modified PET carbon encapsulated in alginate beads for real-world applications, an adsorption experiment was conducted using real water samples collected from two different sources: tap water and

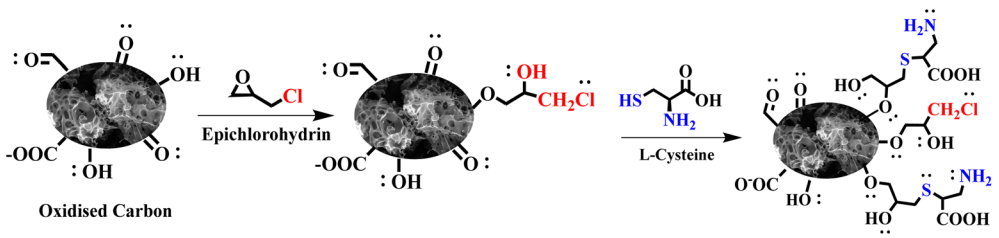

Fig. 12 Mechanistic view of the grafting of L-cysteine.

Table 2 Adsorption performance of the prepared adsorbent in real water samples of tap water and drinking water

Sl. no	Actual concentration of lead (mg L^{-1})	Spiked with lead (mg L^{-1})	Before adsorption (mg L^{-1})	After adsorption (mg L^{-1})	% Adsorption
1	Tap water (0.027)	10	10.32	1.440	86.04
2	Drinking water (0.012)	10	10.62	1.062	90.00

Table 3 Adsorption performance of the prepared adsorbent in a synthetic multi-metal ion solution

Sl. no	Concentration of the metal ions in the prepared synthetic solution	Before adsorption (concentration of Pb^{2+}) (mg L^{-1})	After adsorption (concentration of Pb^{2+}) (mg L^{-1})	% Adsorption
1	Na^+ (50 ppm), Ca^{2+} (50 ppm), Mg^{2+} (10 ppm), K^+ (5 ppm), Pb^{2+} (10 ppm)	13.22	3.040	77.00

drinking water (Table 2). A synthetic multi-ion solution was also prepared, which consisted of Ca^{2+}, Mg^{2+}, Na^+, K^+, and Pb^{2+}. The drinking water, as well as the tap water, was spiked with 10 ppm of lead solution. Analysis was performed using AAS, where the blank in each case was considered by taking the entire solution except for the lead. About 77% of the lead was adsorbed from the synthetic solution. Adsorption was performed by preparing a mixed metal ion solution from their respective salts of the required concentrations, as mentioned in Table 3, in a 500 mL standard flask. 50 mg of adsorbent was added to a conical flask, followed by the addition of 100 mL of the mixed metal ion solution. The flask was equilibrated for 6 h at 250 rpm in an incubator shaker. The obtained results can be ascribed to competitive adsorption and ionic interference from coexisting cations, Ca^{2+} and Mg^{2+}, which compete for the same active sites through electrostatic attraction. As these divalent cations have comparable ionic radii and charge, they partially inhibit Pb^{2+} from coordinating with the functional groups present on the surface of the adsorbent. Furthermore, the increased ionic strength of the solution can compress the electrical double layer, reducing the electrostatic interaction between Pb^{2+} and negatively charged sites on the adsorbent. Even in the presence of competing ions, the retention of 77% adsorption reflects the strong preference of the adsorbent towards Pb^{2+}, due to the soft acid and base interaction between Pb^{2+} and the functional groups present on the surface of the carbon, such as sulphur, oxygen and nitrogen introduced by cysteine modification.

It was observed that the adsorbent exhibited approximately 90% removal efficiency in drinking water, while in tap water, it showed approximately 86% removal efficiency under the same experimental conditions. The decrease in adsorption in the case of tap water could be due to the presence of competing ions in the water, which reduce the available sites for lead to interact. As the concentration of these dissolved ions is lower in drinking water, it exhibits a higher removal efficiency. Lead binding in real samples primarily occurs through chelation and electrostatic interactions between the positively charged lead ions and the negatively charged or electron-donating surface groups of the adsorbent. The slight variation in performance shows that hardness and ionic composition affect adsorption efficiency.

To further investigate the interactions, molecular dynamics simulations were carried out, and the methodology followed is given in the SI (Fig. S6). The MD simulation trajectory revealed two distinct Pb^{2+} binding sites on the cysteine-modified carbon surface. The distance evolution and interaction-energy decomposition collectively reveal a HSAB-consistent, stepwise mechanism for Pb^{2+} coordination at both sites. At binding site 1 (Fig. 14), Pb^{2+} is initially loosely solvated but rapidly drawn

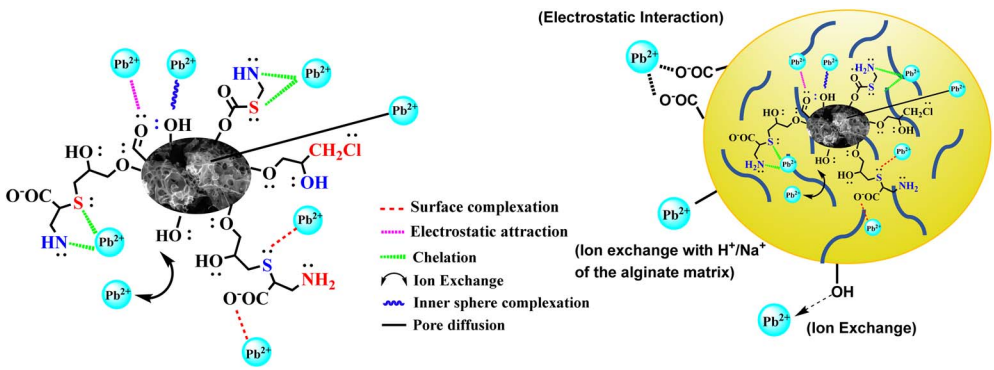

Fig. 13 Possible interactions of the adsorbent with lead.

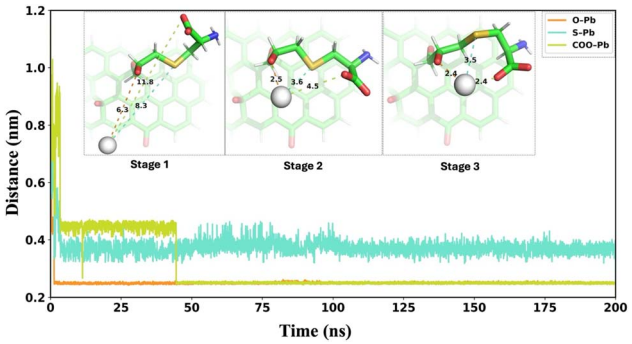

Fig. 14 Time evolution and mechanistic pathway of Pb^{2+} coordination to the L-cysteine functional group (site 1) on carbon during a 200 ns MD simulation.

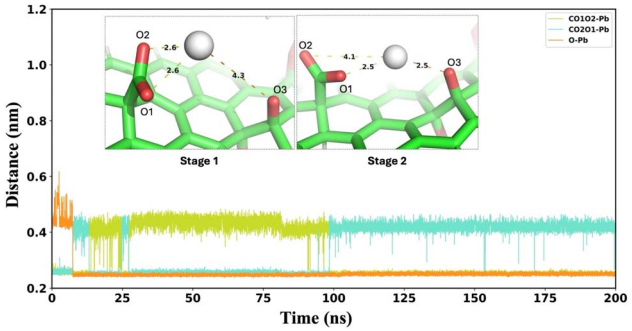

Fig. 15 Time evolution and mechanistic pathway of Pb^{2+} coordination to the carboxylic and hydroxyl functional groups (site 2) on carbon during a 200 ns MD simulation.

toward the surface hydroxyl oxygen, establishing the earliest and most stable O–Pb contact (stage 1). The cysteine sulphur briefly assists in this initial attraction through its lone-pair electrons, but as the ligand backbone relaxes, sulphur is gradually displaced outward due to geometric and steric constraints (stage 2). In parallel, the terminal carboxylate group folds toward the metal centre such that only one of its oxygen atoms forms a persistent inner-sphere interaction with Pb^{2+}, while the second oxygen projects outward toward the solvent (stage 3). This rearrangement produces a well-defined bidentate chelation motif in which hydroxyl oxygen and a single carboxylate oxygen cooperatively bind Pb^{2+}, and this geometry remains stable for the remainder of the 200 ns trajectory.

The interaction-energy analysis corroborates this structural mechanism: oxygen donors overwhelmingly dominate Pb^{2+} stabilisation, consistent with the ion's pronounced oxophilicity under HSAB theory.[43] The hydroxyl oxygen contributes the strongest coulombic interaction (-327.8 kJ mol^{-1}), which is closely followed by the coordinating carboxylate oxygen (-280.0 kJ mol^{-1}). The moderate fluctuations observed in the COO–Pb distance reflect local "breathing" motions of this single coordinating oxygen rather than transitions between the two carboxylate oxygen atoms. In contrast, sulphur contributes only modest stabilisation (-23.7 kJ mol^{-1}), underscoring its transient, early-stage role that is not retained in the optimised binding geometry. Overall, the preference O(hydroxyl) ≈ O(carboxylate) > S results from the interplay of charge distribution, ligand orientation, and metal–ligand hardness/softness compatibility. These findings demonstrate that the oxygen-rich bidentate O···Pb···O–CO coordination motif is principally responsible for strong and persistent Pb^{2+} adsorption at site 1.

At binding site 2, the interatomic distance and interaction-energy analyses reveal a similarly dynamic but selective coordination pathway, with the corrected oxygen assignments showing that O1 and O2 originate from the carboxylate group, while O3 corresponds to the surface hydroxyl oxygen (Fig. 15). At the beginning of the simulation, Pb^{2+} resides closer to one carboxylate oxygen, serving as the primary capture point, which is supported by the high coulombic stabilisation of O1–Pb (-194 kJ mol^{-1}). As the trajectory progresses, the metal ion gradually migrates toward an intermediate position between the carboxylate oxygen and the hydroxyl oxygen (O3), which is

Table 4 Comparison table of various adsorbents used for lead

Sl. No	Adsorbent used	Adsorption capacity (mg g^{-1})	References
1	Sweet potato peels	200.91	44
2	Magnetised activated carbon (MAC)	253.10	45
3	Mg-AL LDH-doped activated carbon	94.60	46
4	Sulphonated biochar	191.07	47
5	Carbon disulphide-modified chitosan resin	204.30	48
6	MOF-graphene oxide composite	232.00	49
7	Cellulose-based ion-imprinted polymer	336.50	50
8	Activated carbon nanoparticle impregnated on lightweight expanded clay	22.83	51
9	FeO_x-modified bone biochar pyrolyzed at 300 °C (FO-BC-300)	173.90	52
10	Chitosan-modified pine wood biochar (CMBC)	134.00	53
11	MW-assisted one-pot synthesis of β-CD-modified biochar (BCMW-β-CD)	240.13	54
12	Modified corn stalks pith biochar by polyethene and potassium hydroxide (SP3)	99.95	55
13	Activated carbon fibres modified with L-cysteine	136	56
14	PVA-L-cysteine composites for multi-metal removal	45.25	57
15	Amidoxime-based mesoporous silica for Pb(II)	242	58
16	Amino-3-mercaptopropionic acid composites	47.25	59
17	MW assisted Ox-PET Carbon@Cysteine alginate beads (this study)	370.84	—

reflected in the progressive shortening of both COO–Pb (O1/O2) and O3–Pb distances. During this transition, the two carboxylate oxygen atoms (O1 and O2) display a characteristic flipping motion. However, the energy decomposition confirms that only one of them (O1) maintains persistent inner-sphere coordination, while O2 exhibits a weaker interaction (-162.9 kJ mol^{-1}) that is consistent with its intermittent, outward-facing orientation. The hydroxyl oxygen (O3) contributes a strong interaction (-334.0 kJ mol^{-1}), confirming its role as the secondary but consistently engaged donor once Pb^{2+} shifts toward the dual-oxygen region. Ultimately, these cooperative interactions generate the same robust O3(hydroxyl)–Pb–O1(carboxylate) bidentate coordination motif observed at site 1, while the second carboxylate oxygen remains non-participatory. Together, the distance traces and energetic contributions indicate that Pb^{2+} binding at site 2 is driven primarily by electrostatic attraction and proceeds through initial carboxylate capture, migration into a dual-oxygen pocket, and final optimisation into an oxygen-dominated bidentate chelation geometry.

3.10 Conclusion

In this study, lead removal was successfully achieved using an adsorbent synthesised from polyethene terephthalate (PET) waste through a microwave-assisted KOH activation route and modified with L-cysteine using epichlorohydrin as a cross-linker, which was then successfully immobilised in alginate beads. The preparation of the adsorbent involves multiple steps. From a scale-up perspective, the carbonisation process was achieved through microwave assistance, which enabled rapid and efficient heating, significantly reducing processing time and minimising energy consumption compared to conventional thermal methods. The oxidation and functionalization processes were also carried out under mild environmental conditions; water was primarily used as a solvent throughout the entire process to impart high-affinity functional groups. The process of alginate encapsulation is also a low-energy consumption process that facilitates its application in fixed beds. Overall, the approach involves a trade-off between process complexity and performance; the combined benefits of using waste PET as a source of carbon, energy-efficient microwave carbonisation, and high adsorption performance support a reasonable balance between functional efficiency and sustainability. The incorporation of chelating functionalities into polymeric and inorganic matrices has been widely explored for heavy metal remediation, including cysteine-functionalized PVA composites, amidoxime-modified mesoporous silica, and pyridine dicarboxyamide-modified chitosan. These adsorbents utilise sulfur, nitrogen, and oxygen-containing ligands to achieve high adsorption capacities. In comparison, the present PET-cysteine@Na-Alg adsorbent employs a distinct strategy by integrating L-cysteine onto a waste PET-derived carbon framework, followed by alginate encapsulation that combines the affinity of thiol-based chelation with the chemical stability of the carbonaceous adsorbent, thereby simultaneously addressing waste valorisation (Table 4). Unlike many polymer-based or silica-based adsorbents that involve only batch adsorption, this adsorbent could be utilised for direct application in fixed-bed columns, offering enhanced stability, facile recovery and reusability. Thus, the innovation of work lies not only in the incorporation of cysteine but also in the synergetic integration of waste-derived carbon and column-compatible architecture. The optimised conditions to achieve maximum adsorption were found to be 370.84 mg g^{-1} as obtained from the adsorption isotherm at pH 7. The zero-point charge of the adsorbent was found to be 6.4 from the pH drift method. The surface area of the adsorbent was found to be 434.67 m^2 g^{-1} of the microwave carbonised carbon and 14 m^2 g^{-1} of the adsorbent. The decrease in surface area was attributed to the oxidation and functionalisation of the carbon. The Langmuir and Freundlich models fitted well, with close regression coefficients, indicating monolayer adsorption with a certain amount of heterogeneity on the adsorbent surface. Kinetics modelling revealed that the adsorption process followed the pseudo-second-order model, suggesting that chemisorption is the rate-limiting step. Additionally, a multi-step adsorption mechanism was observed from the intraparticle diffusion model, which showed a rapid surface uptake of lead ions, followed by gradual pore filling. Thermodynamics further confirmed the feasibility of adsorption, which was exothermic, as indicated by the ΔG° and ΔH° values of -31.44 kJ mol^{-1} and -34.10 kJ mol^{-1}, respectively. Column modelling was performed, from which the maximum adsorption capacity was found to be 245.33 mg g^{-1}. The breakthrough point was achieved at 245.33 min, and the column was saturated at 533 min. Desorption was successfully carried out using 0.1 M NaOH, and the adsorbent exhibited a good adsorption capacity over 5 cycles. The prepared adsorbent was also used to test real-time water samples as well as its adsorption capacity from a synthetic metal ion mixture. Molecular dynamics simulations were successfully carried out. Overall, the study highlights an economical and efficient approach for converting PET waste into a functional, cysteine-modified carbon adsorbent, exhibiting excellent adsorption capacity, selectivity, and reusability for Pb^{2+} removal. This work contributes to the sustainable valorisation of plastic waste and provides a promising route for developing high-performance adsorbents for environmental remediation.

Author contributions

N. Rajesh and Himanshu Aggarwal were involved in conceptualising the work, and K. Krishna Priyanka performed all the experiments related to adsorption. K. Krishna Priyanka and M. Christina Nilavu were involved in acquiring data for all analytical characterisations. Arunraj Balasubramanian was involved in performing the computational studies and interpretations about analytical characterisations and manuscript writing.

Conflicts of interest

The authors declare no conflicts of interest.

Data availability

The datasets generated during and/or analysed during the current study are not publicly available due to confidentiality of

the results but are available from the authors upon reasonable request.

Supplementary information (SI) is available. See DOI: https://doi.org/10.1039/d6su00033a.

Acknowledgements

The authors acknowledge the Central Analytical Laboratory, BITS Pilani, Hyderabad Campus, India, for their support in the analytical characterisation techniques.

References

1 M. De Silva, G. Cao and K. C. Tam, *Environ. Sci.: Nano*, 2025, **12**(4), 2154–2176.
2 X. Long, F. Liu, X. Zhou, J. Pi, W. Yin, F. Li and F. Ma, *Chemosphere*, 2021, **269**, 128698.
3 K. H. H. Aziz, F. S. Mustafa, R. F. Hamarawf and K. M. Omer, *J. Water Proc. Eng.*, 2025, **70**, 106867.
4 A. E. Gahrouei, A. Rezapour, M. Pirooz and S. Pourebrahimi, *Desalination and Water Treat.*, 2024, **319**, 100446.
5 X. Xu, X. Hu, Z. Ding, Y. Chen and B. Gao, *Chem. Eng. J.*, 2017, **308**, 863–871.
6 B. Kaur, J. Singh, R. K. Gupta and H. Bhunia, *J. Environ. Manage.*, 2019, **242**, 68–80.
7 A. Dubey and C. L. Dube, *Nano-Struct. Nano-Obj.*, 2024, **38**, 101136.
8 J. M. Muro-Hidalgo, I. J. Bazany-Rodríguez, J. G. Hernández, V. M. L. Pabello and P. Thangarasu, *J. Fluoresc.*, 2023, **33**(5), 2041–2059.
9 M. Irfan, R. Saleem, B. Shoukat, H. Hussain, S. Shukrullah, M. Y. Naz, S. Rahman, A. A. J. Ghanim, G. Nawalany and T. Jakubowski, *Sci. Rep.*, 2023, **13**(1), 9057.
10 A. A. Joshi and G. Ragupathy, *RSC Adv.*, 2025, **15**, 34609–34634.
11 N. Mojoudi, N. Mirghaffari, M. Soleimani, H. Shariatmadari, C. Belver and J. Bedia, *Sci. Rep.*, 2019, **9**(1), 19352.
12 N. B. Mohamed, N. Ngadi, S. Wong, N. Y. Yahya, O. Hassan, I. M. Inuwa, L. A. Opotu and N. Ali, *Sci. African*, 2022, **16**, e01135.
13 A. Kassem, L. Abbas, O. Coutinho, S. Opara, H. Najaf, D. Kasperek, K. Pokhrel, X. Li and S. Tiquia-Arashiro, *Front. Microbiol.*, 2023, **14**, 1304081.
14 C. Das, N. N. Ghosh, V. Pulhani, G. Biswas and P. Singhal, *RSC Adv.*, 2023, **13**, 15015–15023.
15 B. Wang, J. Lan, C. Bo, B. Gong and J. Ou, *RSC Adv.*, 2023, **13**(7), 4275–4302.
16 V. Algieri, A. Tursi, P. Costanzo, L. Maiuolo, A. De Nino, A. Nucera, M. Castriota, O. De Luca, M. Papagno, T. Caruso and S. Ciurciù, *Chemosphere*, 2024, **355**, 141891.
17 Y. Zheng, P. Lv, J. Yang and G. Xu, *ACS Omega*, 2023, **8**(33), 29966–29978.
18 O. A. Alnasra, F. I. Khalili and F. A. Alhnafat, *Desal. and Water Treat*, 2024, **320**, 100604.
19 M. U. Dao, H. S. Le, H. Y. Hoang, V. A. Tran, V. D. Doan, T. T. N. Le, A. Sirotkin and V. T. Le, *Environ. Research*, 2021, **198**, 110481.
20 Y. Guo and Q. Wang, *Processes*, 2022, **10**(9), 1712.
21 X. Zhou, Y. Liu, C. Jin, G. Wu, G. Liu and Z. Kong, *RSC Adv.*, 2022, **12**, 1130–1140.
22 Q. Liu, J. Huang, J. Zhang, Y. Hong, Y. Wan, Q. Wang, M. Gong, Z. Wu and C. F. Guo, *ACS Appl. Mater. Interfaces*, 2018, **10**, 2026–2032.
23 X. L. Sun, Z. Liu and Z. L. Cheng, *J. Alloys Compd.*, 2021, **885**, 160976.
24 L. Zhang, S. Tang, F. He, Y. Liu, W. Mao and Y. Guan, *Chem. Eng. J.*, 2019, **378**, 122215.
25 A. Bakandritsos, P. Hobza, R. Zbořil, J. Kolařík, Z. Bad'ura, R. Lo, G. Zoppellaro, Š. Kment, A. Naldoni, Y. Zhang, M. Petr, O. Tomanec, J. Filip and M. Otyepka, *ACS Nano*, 2021, **15**, 3349–3358.
26 Y. Liao, Y. Wang, X. Zhu and G. Ji, *Environ. Technol. Innovat.*, 2021, **23**, 101580.
27 P. L. Yap, Y. L. Auyoong, K. Hassan, F. Farivar, D. N. Tran, J. Ma and D. Losic, *Chem. Eng. J.*, 2020, **395**, 124965.
28 M. Iqbal, J. Nisar, M. Adil, M. Abbas, M. Riaz, M. A. Tahir, M. Younus and M. Shahid, *Chemosphere*, 2017, **168**, 590–598.
29 M. Vescovi, M. Melegari, C. Gazzurelli, M. Maffini, C. Mucchino, P. P. Mazzeo and D. Rogolino, *RSC Sustain.*, 2023, **1**(6), 1423–1435.
30 A. A. Abdel Hafez, H. S. M. Abd-Rabboh, A. M. Al-Marri and A. H. A. Aboterika, *ACS Omega*, 2023, **8**, 42622–42631.
31 H. Wu, W. Zhang, H. Zhang, Y. Pan, X. Yang, Z. Pan and X. Yu, *Colloids Surf. A.*, 2020, **607**, 125517.
32 R. Karthik and S. Meenakshi, *Int. J. Biol. Macromol.*, 2014, **67**, 210–219.
33 J. Febrianto, A. N. Kosasih, J. Sunarso, Y. H. Ju, N. Indraswati and S. Ismadji, *J. Hazard Mater.*, 2009, **162**(2–3), 616–645.
34 J. S. Piccin, G. L. Dotto and L. A. A. Pinto, *Braz. J. Chem. Eng.*, 2011, **28**, 295–304.
35 B. Liu, H. Luo, H. Rong, X. Zeng, K. Wu, Z. Chen, H. Lu and D. Xu, *Desalination Water Treat.*, 2019, **160**, 260–267.
36 S. Paul, A. J. Gogoi, K. Dev, P. P. Handique, D. B. Bora, S. Kalita and R. Borah, *RSC Sustain.*, 2024, **3**, 486–502.
37 N. B. Mohamed, N. Ngadi, S. Wong, N. Y. Yahya, O. Hassan, I. M. Inuwa, L. A. Opotu and N. Ali, *Sci. Afr.*, 2022, **16**, 01135.
38 O. B. Omitola, M. N. Abonyi, K. G. Akpomie and F. A. Dawodu, *Water Sci. Appl.*, 2022, **12**(5), 94.
39 C. Yang, H. Shang, J. Li, X. Fan, J. Sun and A. Duan, *Processes*, 2023, **11**(5), 1487.
40 S. Y. Yang, B. C. Bai and Y. R. Kim, *Surfaces*, 2023, **7**(1), 12–25.
41 G. Bayramoglu, I. Gursel, M. Yilmaz and M. Y. Arica, *J. Chem. Technol. Biotechnol.*, 2012, **87**(4), 530–539.
42 T. A. Le and T. P. Huynh, *Eur. Polym. J.*, 2023, **184**, 111852.
43 K. P. Kepp, *Inorg. Chem.*, 2016, **55**(18), 9461–9470.
44 O. Chidi and R. Kelvin, *Chem. Int.*, 2018, **4**(4), 221–229.
45 Z. Zhang, T. Wang, H. Zhang, Y. Liu and B. Xing, *Sci. Total Environ.*, 2021, **757**, 143910.
46 A. K. Khalil, I. W. Almanassra, A. Chatla, I. Ihsanullah, T. Laoui and M. A. Atieh, *Chem. Eng. Sci.*, 2023, **281**, 119192.
47 W. Yu, J. Hu, Y. Yu, D. Ma, W. Gong, H. Qiu, Z. Hu and H. W. Gao, *Sci. Total Environ.*, 2021, **750**, 141545.

48 L. Chen, K. Wu, M. Zhang, N. Liu, C. Li, J. Qin, Q. Zhao and Z. Ye, *Chem. Eng. J.*, 2023, **466**, 143082.
49 T. Chowdhury, L. Zhang, J. Zhang and S. Aggarwal, *Adv. Mater.*, 2021, **2**, 3051–3059.
50 M. S. Aljohani, R. B. Alnoman, H. Y. Alharbi, M. Al-Anazia and M. Monier, *Int. J. Biol. Macromol.*, 2024, **259**, 129145.
51 A. Ghahremani, M. Manteghian and H. Kazemzadeh, *J. Environ. Chem. Eng.*, 2021, **9**(1), 104478.
52 J. Xiao, R. Hu, G. Chen and B. Xing, *J. Hazard. Mater.*, 2020, **399**, 123067.
53 N. B. Dewage, R. E. Fowler, C. U. Pittman, D. Mohan and T. Mlsna, *RSC Adv.*, 2018, **8**, 25368–25377.
54 J. Qu, M. Dong, S. Wei, Q. Meng, L. Hu, Q. Hu, L. Wang, W. Han and Y. Zhang, *Carbohydr. Polym.*, 2020, **250**, 117003.
55 S. Fan, Y. Sun, T. Yang, Y. Chen, B. Yan, R. Li and G. Chen, *RSC Adv.*, 2020, **10**, 6362–6376.
56 L. Zhu, Y. Yao, D. Chen and P. Lan, *RSC Adv.*, 2022, **12**, 20062–20073.
57 S. A. Mahmoud, B. M. Atia and M. Abdalla, *ChemistrySelect*, 2024, **9**(26), e202401169.
58 M. Mohery, G. M. Mahran, B. M. Atia and M. A. Gado, *Inorg. Chem. Commun.*, 2025, **180**, 114884.
59 S. A. Mahmoud, B. M. Atia and M. A. Gado, *Int. J. Environ. Sci. Technol.*, 2025, **22**, 12269–12294.